Pergamon

Int. J. Heat Mass Transfer. Vol. 38, No. 14, pp. 2519–2527, 1995

0017-9310/95 $9.50+0.00

0017-9310(95)00018-6

Mixed convection in horizontal channels with discrete material and top exhaust

T. L. BERGMAN and Y. S. SON

Department of Mechanical Engineering, The University of Texas at Austin, Austin, TX 78712, U.S.A.

(*Received* 1 *July* 1994 *and in final form* 27 *December* 1994)

Abstract—Mixed convection in a horizontal channel loaded with discrete material and equipped with a top exhaust was studied experimentally and analytically. The steady flow was two-dimensional 2D, while observed unsteady convection, triggered at a critical Richardson value, was highly three-dimensional 3D. Measured temperatures and those predicted with a 2D numerical model are in good agreement. The model, however, underestimates the onset of the thermally-induced transition to unsteady convection.

INTRODUCTION

Various heating operations are performed in which the discrete product (which may be stationary or moving) is warmed, as shown in Fig. 1. Examples include enameling, annealing, baking and reflow soldering. A typical oven configuration involves air as the working fluid, with exhaust(s) used to control convective heating and/or expel fumes from the processed material. To predict the material's thermal response, it is necessary to quantify convective heat transfer rates. Convection is, in general, mixed because of co-existence of thermal buoyancy forces, possible material motion and exhaust-induced flow.

Several features distinguish the mixed convection here from that in studies involving (i) channel flow with destabilizing buoyancy forces [1] or (ii) continuous moving material [2]. Obviously, the main oven flow is not unidirectional, but varies relative to the exhaust position. The discrete material redistributes oven temperatures in a conjugate manner, and the exhaust induces a vertical velocity component. In practice, solids or gaps exist beneath the exhaust if the material moves on a porous conveyor, inducing time-periodic behavior.

Because of the expense of full 3D transient simulation in industrial ovens (especially in cases where radiation is significant relative to mixed convection heat transfer rates), it is desirable to incorporate 2D modeling (no variation in the spanwise direction), and this strategy has been taken for systems where the third oven and product dimensions are large [3,4]. The issue becomes, then, whether the 2D flow assumption is appropriate in the face of a large body of literature which suggests that, in general, the convection is 3D [see refs. in 1]. A cursory inspection of the geometry in Fig. 1 suggests that the flow may tend to two-dimensionality because of the discrete plates and a top-mounted exhaust. That is, the induced vertical velocities may induce up flow (down flow) between the material which, in turn, may modify 3D steady vortical structures to a 2D mode.

In this study, experiments were performed in conjunction with numerical modeling to observe and predict steady and oscillatory convection. Because of (i) the number of relevant length scales associated with discrete material loading (exhaust number, size and location, as well as material thickness, length, elevation and gap size) and (ii) the range of operating conditions which might be encountered (exhaust and material velocities), it is impossible to consider all

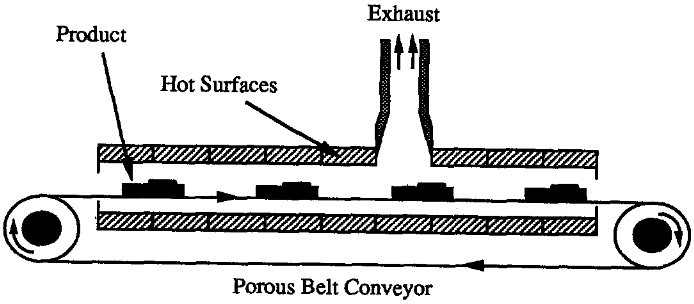

Fig. 1. Schematic of a processing oven loaded with discrete material.

NOMENCLATURE

A_c	cross-sectional area
Gr	Grashof number, $g\beta(T_b - T_t)H^3/\nu^2$
g	gravitational acceleration
h	computational domain vertical length, convection coefficient
H	channel height
k	thermal conductivity
l	computational domain horizontal length
P	exposed perimeter
Re	Reynolds number, $U_m \cdot H/\nu$
Ri	Richardson number, Gr/Re^2
T	temperature
U_m	mean velocity
x, y	horizontal coordinate, vertical coordinate
x^*	horizontal coordinate relative to the test section.

Greek symbols

β	thermal expansion coefficient, grid expansion factor
ε	emissivity
ν	kinematic viscosity
σ	Stefan–Boltzmann constant
θ	dimensionless temperature, $(T - T_\infty)/(T_{avg} - T_\infty)$
θ^*	dimensionless temperature, $(T - T_\infty)/(T_{max} - T_\infty)$.

Subscripts

avg	$(T_t + T_b)/2$
b, t	bottom heat exchanger, top heat exchanger
c	critical
HE	heat exchanger
l, r	left, right
max	maximum
∞	ambient.

combinations of potentially relevant parameters in a general study. The motivation for selecting the conditions here is soldering of electronic components which occurs in ovens of approximately 50 mm height with mean air flow velocities at least an order of magnitude greater than the material velocity [4]. The limiting case of stationary material is considered here.

EXPERIMENTS

The apparatus is shown in Fig. 2. A fan draws air from a horizontal test section whose interior dimensions are shown. The test section houses stationary solid plates which are suspended between top and bottom, constant temperature walls. The exhaust air is replenished by flow from the left and right, which is delivered from separate entrance sections whose lengths exceed that required for fully-developed hydrodynamic flow. Straightened (using banks of packed drinking straws) room temperature air is delivered to the entrance sections via separate settling chambers, each housing four flow straightening banks. The air flow rate into each entrance section is determined at a measuring station. During experiments, the entire system is wrapped in styrofoam insulation. Of course, mixed convection due to material motion cannot be investigated here, and the relevance of the study is limited to processes where stationary material or small conveyor velocities are used.

The 762 mm long, 30 mm tall, 381 mm deep test section and the two 500 mm long entrance sections are shown in Fig. 3. The entrances, as well as the vertical test section walls, are made of 6.35 mm thick acrylic plate. Heat exchangers form the test section ceiling and floor, and are fabricated of 22.25 mm thick polished aluminum plate with internal serpentine coolant channels which are, in turn, supplied by separate Haake A82 constant temperature circulators. Stationary plates (consisting of two sandwiched 3.5 mm aluminum sheets bonded with double-sided tape) are installed slightly below the channel mid-height via notches milled into the side walls. The variable speed exhaust fan (Fig. 2) is connected to two 12.7 mm diameter PVC tubes (perforated with 4 mm diameter holes and connected in series) which span the channel depth and promote 2D exhaust flow.

The flow rates are small ($15 \leqslant U_m < 50$ mm s^{-1}), inducing very small pressure drops throughout the apparatus. Pressure drops across the orifice plates were measured with Omega PX653 transducers (accuracy of ± 0.015 mm H_2O) and the pressure drop was related to U_m via off-line calibration. Reference flow rates in the calibration were measured with a Dwyer RMC-102 rotameter.

Twelve 0.13 mm T-type thermocouples were taped into each aluminum plate (uniformly dispersed about the plate's projected area), and the same type thermocouples were used to measure the incoming air temperature (inside the settling chambers), the heat exchanger temperatures (six thermocouples per heat exchanger), mid-span air temperatures at locations shown in Fig. 3 (butt-welded thermocouples were stretched across the channel width), and the entrance section surface temperatures at relative distances of 50 and 400 mm from the test section. The last temperature measurement was made to check for conjugate preheating of the incoming air (which is significant). All thermocouples were made from the same wire role, minimizing experimental uncertainty.

Flow visualization was performed by injecting

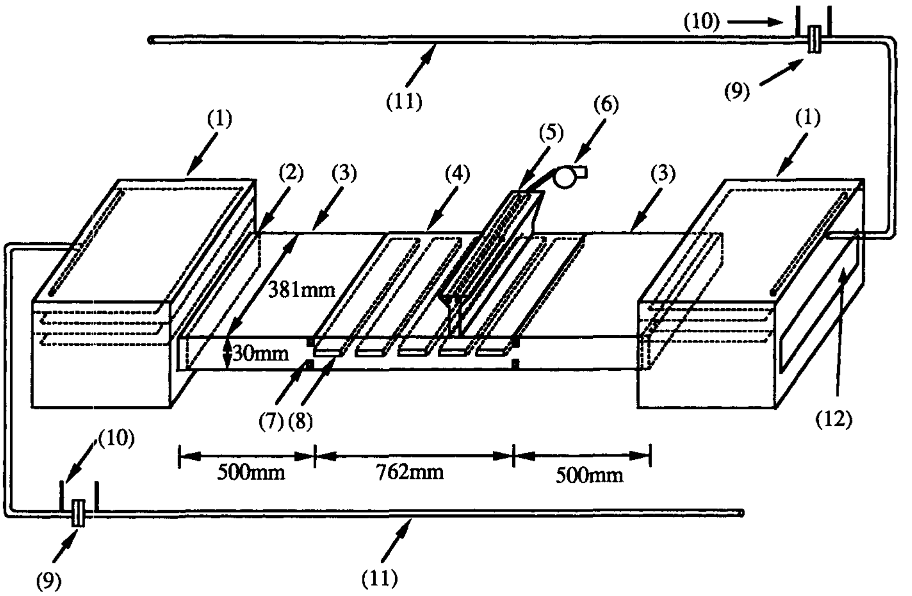

(1) Settling Chambers, (2) Flow Straightener (typ.), (3) Entrance Sections, (4) Test Section (5) Exhaust Duct, (6) Fan, (7) Baffle, (8) Plate (typ.), (9) Orifices, (10) Pressure Taps, (11) Inlets, (12) Window

Fig. 2. The experimental apparatus.

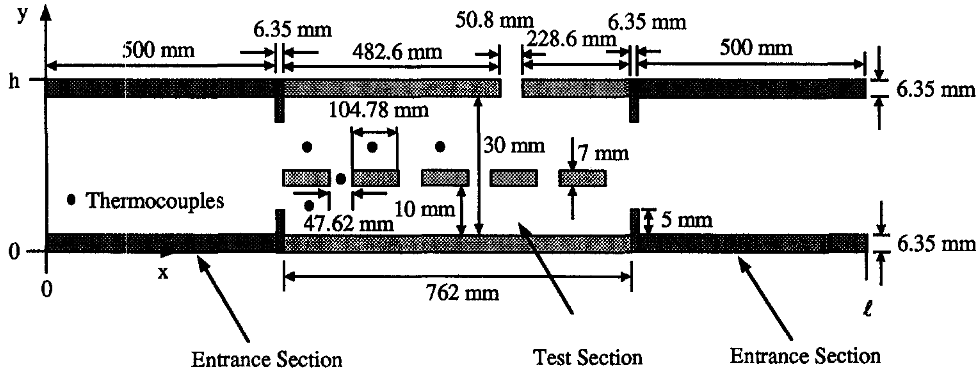

Fig. 3. Side view of the entrance and test sections. Thermocouples are located 5 mm above and below the plate surfaces at the plate horizontal center lines, as well as midway between plates 1 and 2 at the plate vertical center line.

room-temperature incense smoke into a gap between the straws, and illuminating the stream with a He–Ne laser and cylindrical lens. The maximum lateral shift of the smoke line (injected approximately 20 mm from the side wall) was estimated to be 10 mm over 880 mm of streamwise travel, under isothermal conditions. Smoke injected at mid-span and mid-height did not noticeably drift over the same travel distance, again under isothermal conditions. It is emphasized that, relative to studies involving heated channels with no material loading, flow visualization is difficult since (i) optical access is limited by the loaded opaque material and (ii) the surfaces are polished to a near mirror finish to reduce their emissivity, resulting in significant reflection of the laser light and smoke images.

A Hewlett–Packard 3497A data acquisition unit, coupled to an IBM PC-AT, was used to monitor the air flow rate and various temperatures. Typically, the experiments required 24 h to reach a steady state (defined as a state when all plate temperatures change by less than 0.05°C over a 30-min interval). The temperatures within an individual plate differed by no more than 0.4°C. The data were corrected for radiation exchange (see the Appendix) and an uncertainty analysis [5] yielded $u_{\mathrm{Re}} = \pm 2.5$, $u_{\mathrm{Gr}} = \pm 160$, $u_{\mathrm{Ri}} = \pm 15\%$ and $u_\theta = \pm 0.012$. Here, u_θ is associated with the uncorrected value of θ.

NUMERICAL MODEL

The computational domain ($0 \leqslant x \leqslant l, 0 \leqslant y \leqslant h$) is shown in Fig. 3 and encompasses the oven air, stationary plates, heat exchangers, and the acrylic entrance section walls. Two-dimensional, unsteady convection is assumed, in conjunction with 2D unsteady conduction in the plates. The governing equations involve mass, momentum and thermal energy conservation, and are listed elsewhere [3–5]. Constant properties are assumed here (except in the y momentum source term) and radiation is neglected.

A finite volume method with a non-staggered grid was used to solve the discretized forms of the governing equations, and the solution procedure is outlined elsewhere [5]. As is well known, use of the FVM (in conjunction with harmonic mean averaging of transport properties) simplifies treatment of the embedded solids [6] whose velocities are set to zero.

At $x = 0$ and l, uniform air velocity distributions are assigned. The mean mass flow is the measured left or right value. At the exhaust ($y = h$) a parabolic velocity profile is specified, with the mean flow set to the sum of the measured left and right entrance values. Air enters at T_∞ while $\partial T/\partial y$ is set to zero at the exhaust. The exteriors of all solid surfaces (bounded by $y = 0$ and h) are adiabatic.

Heat exchanger control volume temperatures are set to the measured values. The entrance section wall temperature distribution was estimated by using an infinite fin analysis [7] and neglecting the contact resistance at the test-entrance section flange,

$$T = T_\infty + (T_{\mathrm{HE}} - T_\infty)\exp(-mx^*) \qquad (1)$$

where $m = (hP/kA_c)^{1/2}$ and h is determined from the fully developed 2D laminar flow analysis [8]. Specified and measured entrance section wall temperatures are in good agreement, and use of equation (1) raises predicted θ of the 1st and 5th plates by approximately 75% (into good agreement with measured values) [5]. Use of equation (1) does not significantly affect the predicted θ of plates 2–4, relative to predictions based upon the assumption of no heat transfer in the entrance section wall.

Because the response is slow, simulations were speeded (by an estimated order of magnitude) with an iterative procedure. Specifically, the plate temperatures were each assumed, and the simulation proceeded until the time-averaged behavior was invariant. The time-averaged convective heat transfer to each plate was evaluated, and the plate temperature was adjusted until zero net heat transfer was predicted. Typically, 10 iterations were necessary.

The simulations were performed using $\Delta t = 0.0025$ s and a 298×57 mesh. A uniform grid was used in the x direction within the test section (238 control volumes), while a smoothly-variable grid size ($\beta = 1.03$) [9] is used in the entrance sections (coarse resolution near $x = 0$, l). Fine mesh was used near solid surfaces, and within the plates in the y direction, leaving relatively large control volumes at $y/h \approx 0.3$ and 0.7. In y, $\beta = 1.15$ was used. Predicted plate temperatures are time step and grid size independent. Time-averaged air temperatures are also time step and grid size independent, although fluctuation amplitudes and frequencies are not. Each simulation required approximately 10 days CPU time on an IBM RS 6000 workstation, and details of the numerical sensitivity studies are available elsewhere [5].

RESULTS

Experimental conditions are listed in Table 1 in order of increasing Ri (transitions to unsteady convection have been, in the main, related to Ri [1]). A transition to unsteady convection (as deduced by flow visualization and measured local air temperature fluctuations) occurs in the range $36 \leqslant Ri \leqslant 46$. Because three characteristic temperatures exist (T_t, T_b and T_∞), at least three different Ri could be defined. However, the transition coincided only with Ri based upon $T_b - T_t$ and H [5], implying that unstable buoyancy forces within the core of the test section lead to fluctuating behavior.

Steady state

Two-dimensional flow was visually observed in each steady state experiment. Several predicted test

Table 1. Experimental conditions

Case	T_t [°C]	T_b [°C]	U_l [mm s^{-1}]	U_r [mm s^{-1}]	Re	$Gr \times 10^{-4}$	Ri	Comment
A	50	25	15.5	16.4	30	−8.2	−90	Steady
B	30	35	15.7	16.6	31	−1.65	−18	Steady
C	50	25	49.8	50.2	92	−8.2	−10	Steady
D	40	35	50.7	51.3	95	−1.65	−2	Steady
E	37.5	37.5	15.7	16.6	31	0	0	Steady
F	37.5	37.5	51.0	51.7	95	0	0	Steady
G	60	60	19.3	20.4	35	0	0	Steady
H	35	40	50.7	51.2	94	1.65	2	Steady
I	25	50	50.7	51.2	94	8.2	9	Steady
J	35	40	15.8	16.8	31	1.65	17	Steady
K	45	60	19.3	20.4	36	4.37	34	Steady
L	25	60	30.3	30.5	55	11.0	36	Steady
M	40	60	19.3	20.4	37	5.9	46	Unsteady
N	25	60	24.7	25.0	45	11.0	54	Unsteady
O	25	60	19.3	20.4	37	11.0	81	Unsteady
P	25	50	15.6	16.6	31	8.2	88	Unsteady

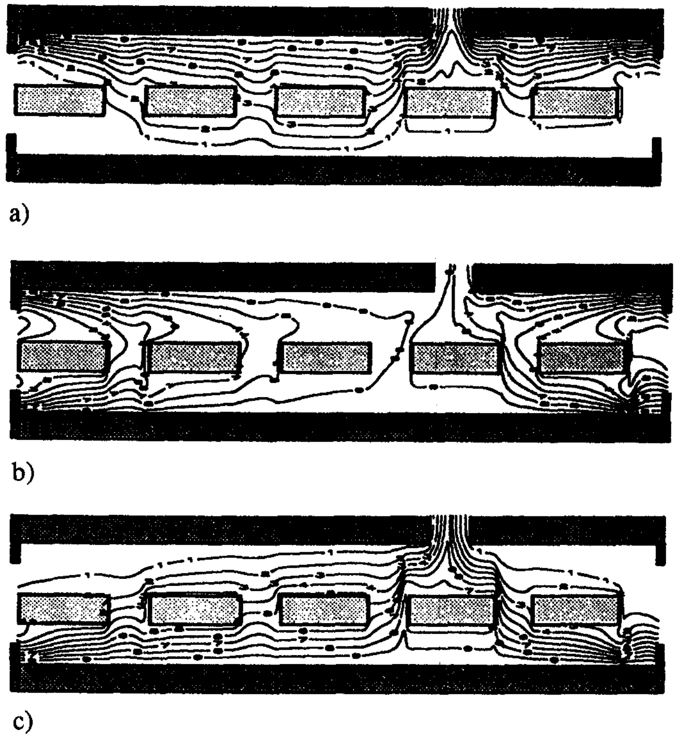

Fig. 4. Predicted test section temperature distributions for (a) $Ri = -10$, (b) $Ri = 0$, $Re = 95$ and (c) $Ri = 9$ cases. Contour values are for $\theta^* \cdot 10$.

section temperature distributions at $Re \approx 90$ are shown in Fig. 4. The figure has been expanded vertically by a factor of 5, making interpretation of velocity distributions difficult. In each case, $T_{avg} = 37.5°C$, and temperatures are shown at $0.1 \leqslant \theta^* \leqslant 0.9$ in increments of 0.1.

Thermal stratification is noted in Fig. 4(a), with warm air traveling in the upper half of the channel until it is expelled from the system. The bottom channel half is relatively cool. In contrast, Fig. 4(c) shows warm air rising from the bottom surface induced by buoyancy forces and exhaust-induced up flow. For symmetric thermal boundary conditions, Fig. 4(b), relatively uniform warm air in the vicinity of the exhaust is noted. Overall, slightly greater horizontal velocities exist above the plates due to the flow resistance posed by the gaps between the plates.

Predicted and measured temperatures are shown in Fig. 5 for the $Re \approx 90$, $T_{avg} \approx 37.5°C$ cases. Predicted temperatures along $y = 19.85$ mm (center of the plates) are shown. Excellent qualitative agreement exists between the measurements and predictions, with higher (cooler) temperatures associated with the warmer (cooler) T_b. The average absolute difference

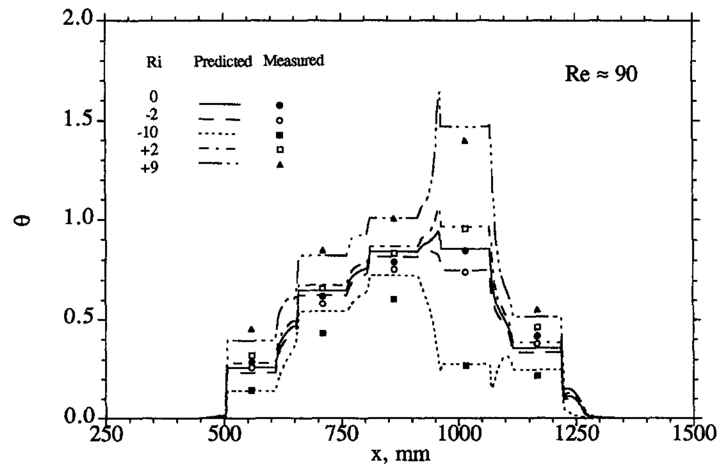

Fig. 5. Predicted and measured temperatures for the $Re \approx 90$ steady state cases.

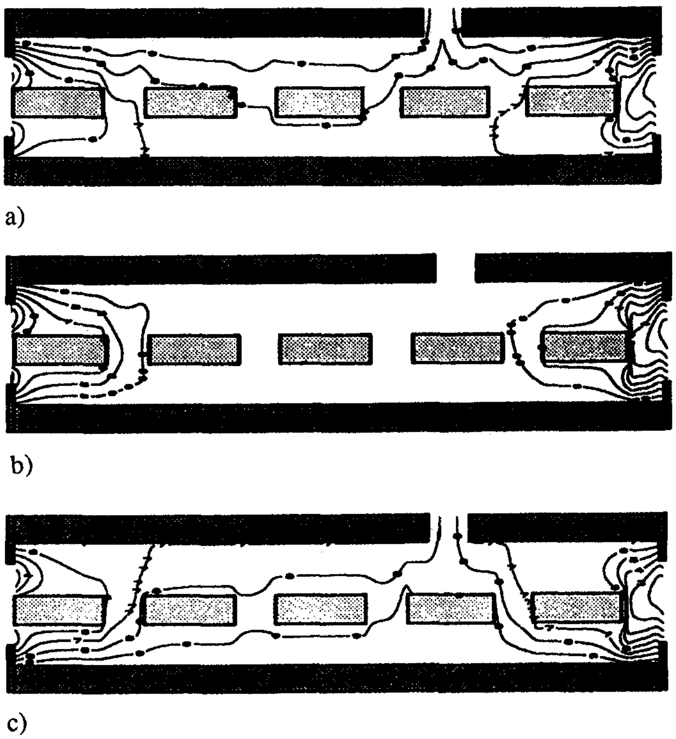

Fig. 6. Predicted test section temperature distributions for (a) $Ri = -18$, (b) $Ri = 0$, $Re = 31$ and (c) $Ri = 17$ cases. Contour values are for $\theta^* \cdot 10$.

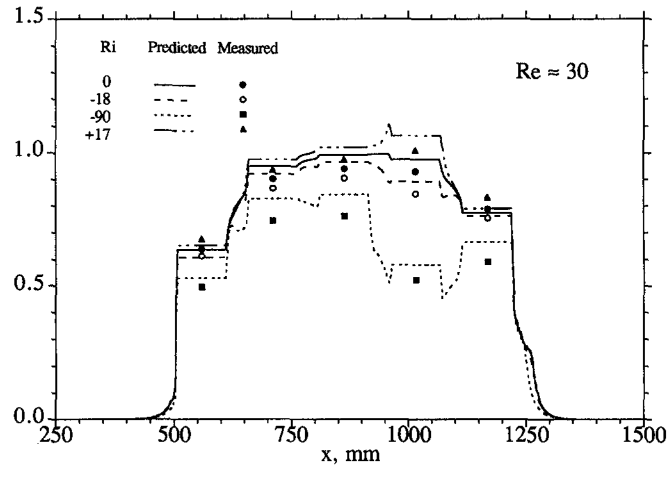

Fig. 7. Predicted test section temperature distributions for the $Re \approx 30$ steady state cases.

between predicted and measured material temperatures, normalized by the measured material temperature, is 7%.

Several predicted test section θ^* distributions are shown in Fig. 6 for the $Re \approx 30$ cases. As in Fig. 4, $T_{avg} \approx 37.5°C$, and air temperatures are shown in θ^* spanning from 0.1 to 0.9 in increments of 0.1. A comparison of Figs. 4(b) and 6(b), for example, shows the influence of reduced mean velocities, with a large warm region in the low velocity case. Similar stratification phenomena are noted as in the high Re cases, with imposition of extreme thermal conditions ($Gr = 8.2 \times 10^4$) triggering oscillatory convection in the low velocity case.

Measured and predicted temperatures ($Re \approx 30$, $T_{avg} \approx 37.5°C$) are reported in Fig. 7, with warmer overall temperatures again associated with warm bottom heat exchanger temperatures. The temperature range for the plate directly beneath the exhaust is reduced relative to the high velocity case. As for the $Re \approx 90$ cases, agreement between measurement and predictions is quite good. The average absolute

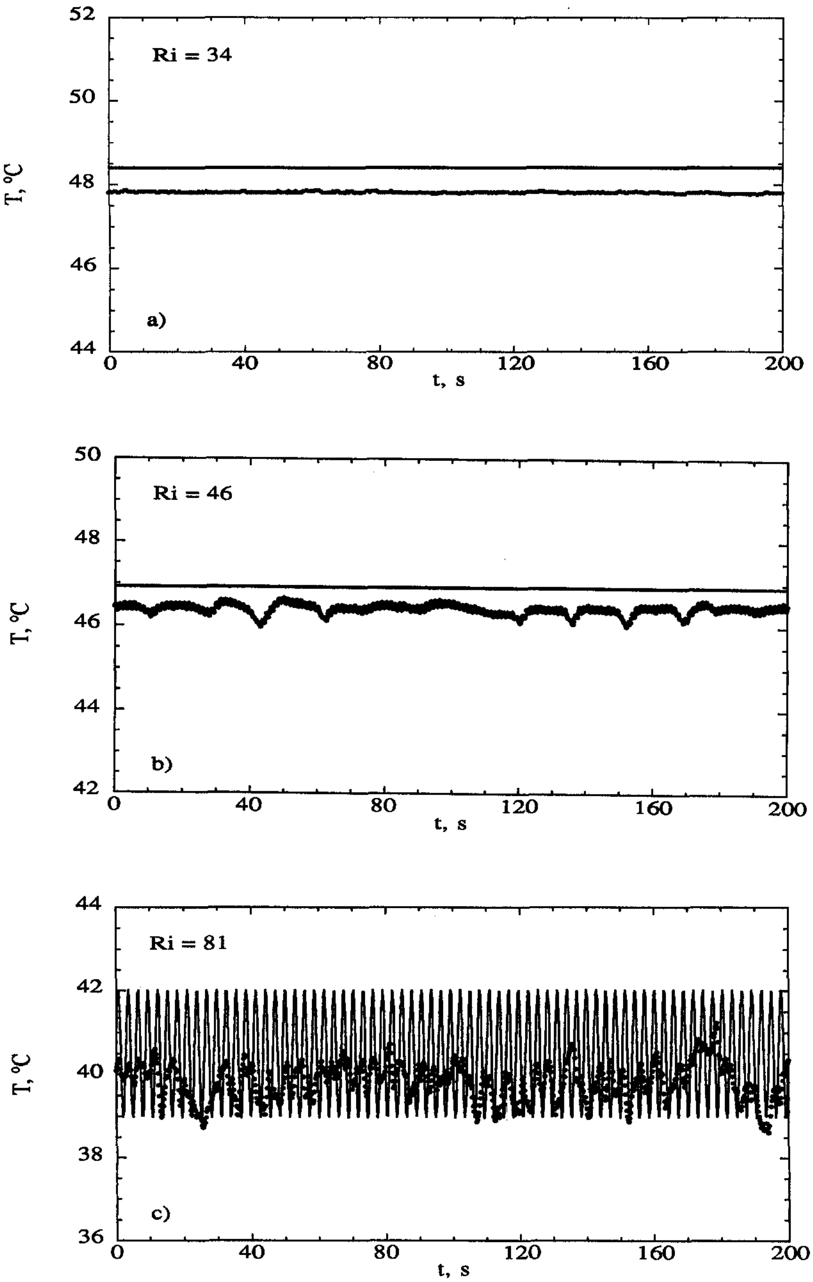

Fig. 8. Measured and predicted local air temperature distributions (for the location above the 3rd plate) for (a) $Ri = 34$, (b) $Ri = 46$ and (c) $Ri = 81$ cases.

difference between predicted and measured material temperatures, normalized by the measured material temperature, is 5%.

Oscillatory convection

Three-dimensional convection, consisting of a complex mixture of unsteady spanwise and streamwise structure, was noted visually for each oscillatory case. The onset of the instability could also be determined by inspection of the air temperature measurements. As Ri is increased, the instability was first noted above the 2nd and 3rd plates. At higher Ri, the instability propagates to the gap separating the 1st and 2nd plates, with stable flow noted in all experiments above and below the 1st plate.

Figure 8 shows measured and predicted temperatures above the 3rd plate for $Ri = 34$, 46 and 81. Measured and predicted mean air temperatures are in good agreement (within 3%), as in every case of the study. Steady convection was measured and predicted for $Ri \leqslant 36$. Unsteady convection was noted experimentally at $Ri = 46$ and 54, but the predictions indicate steady flow for these cases. Predicted and measured temperatures fluctuate for $Ri \geqslant 81$ cases. An

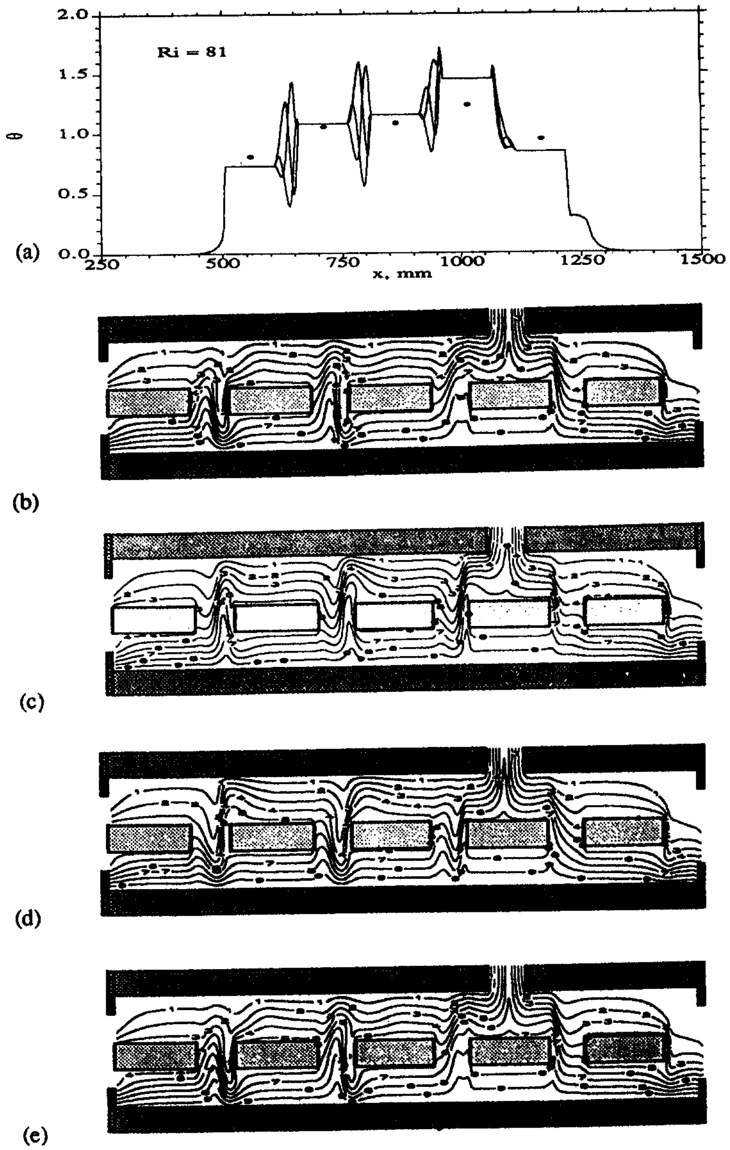

Fig. 9. Measured and predicted test section temperatures for the $Ri = 81$ case (a), along with predicted air temperature distributions at relative times of (b) 0, (c) 1, (d) 2 and (e) 3 s. Contour values are for $\theta^* \cdot 10$.

additional simulation was performed with $Ri = 41$, $Gr = 11 \times 10^5$ and $Ri = 66$, resulting in fluctuating flow. In summary, the experiments revealed $36 \leqslant Ri_c \leqslant 46$ while the simulations indicated $54 \leqslant Ri_c \leqslant 66$. Since the fluctuating flow is highly 3D just beyond transition, it is not surprising that the 2D model yields higher Ri_c.

Finally, a comparison of measured and predicted temperatures is shown in Fig. 9(a) for the $Ri = 81$ case, with predictions shown at relative times of 0, 1, 2 and 3 s. The average absolute difference between predicted and measured material temperatures, normalized by the measured material temperature, is 9%. As evident in Figs. 9(b)–(e), the flow field oscillates with up flow and down flow occurring intermittently between the plates. In a manner consistent with the measured local air temperatures, little activity is noted above and below the first (or fifth) plate.

SUMMARY AND CONCLUSIONS

This study has shown that, for the geometry and operating conditions considered, 2D (no spanwise variation) mixed convection is the dominant mode when steady conditions are present. Upon triggering into an oscillatory mode, highly 3D flow was observed. Because the steady convection is 2D, the two-dimensional model performs well in predicting temperatures within the system. Even in unsteady 3D flow, the numerical predictions are surprisingly close to the measured time-mean air and plate temperatures. The onset of oscillatory convection correlated well with *Ri*, even though a variety of length scales and temperature differences exist within the system.

Obviously, the scope of the investigation is limited, considering the array of configurations and applied thermal boundary conditions which could be studied. For example, different orientations relative to the gravitational acceleration vector could be considered. The presence of multiple or bottom exhausts, different plate placement relative to the exhaust or to each other, and moving material may induce different convective behavior. In any of these cases, however, the discrete material loading, in conjunction with the top exhaust, is expected to modify significantly the mixed convection modes present, and 2D modeling may be appropriate for a variety of practical configurations.

REFERENCES

1. C. C. Huang and T. F. Lin, Buoyancy induced flow transition in mixed convective flow of air through a bottom heated horizontal rectangular duct, *Int. J. Heat Mass Transfer* **37,** 1235–1255 (1994).
2. S. R. Choudhury and Y. Jaluria, Analytical solution for the transient temperature distribution in a moving rod or plate of finite length with surface heat transfer, *Int. J. Heat Mass Transfer* **37,** 1193–1205 (1994).
3. T. L. Bergman, M. A. Eftychiou and G. Y. Masada, Thermal processing of discrete, conveyorized material. In *Heat Transfer in Materials Processing* (Edited by J. C. Kanpara and P. Bishop), HTD-Vol. 224, pp. 27–34. ASME, New York (1992).
4. M. A. Eftychiou, T. L. Bergman and G. Y. Masada, A detailed model of the infrared reflow soldering process, *J. Electron. Packaging* **115,** 55–62 (1993).
5. Y. S. Son, Multimode heat transfer during reflow soldering of electronics assemblies, Ph.D. Thesis, The University of Texas at Austin, Austin, TX (1994).
6. S. V. Patankar, *Numerical Heat Transfer and Fluid Flow* (1st Edn), p. 149. McGraw-Hill, New York (1980).
7. F. P. Incropera and D. P. DeWitt, *Fundamentals of Heat and Mass Transfer* (3rd Edn), p. 127. Wiley, New York (1990).
8. W. M. Kays and M. E. Crawford, *Convective Heat and Mass Transfer* (2nd Edn), p. 103. McGraw-Hill, New York (1980).
9. D. A. Anderson, J. C. Tannehill and R. H. Pletcher, *Computational Fluid Mechanics and Heat Transfer*, pp. 248–251. Hemisphere, Washington, DC (1984).

APPENDIX

Because the convective heat transfer rates are small, the measured plate temperatures were corrected to account for radiative exchange. To do so, the emissivity of the polished aluminum surfaces was estimated by viewing the heat exchanger surfaces (prior to assembling the test section) with an Inframetrics Model 600 thermal camera operating in the 8–12 μm range. Warm circulating fluid was pumped through the exchangers, and their temperatures were measured with the embedded thermocouples. With knowledge of the surrounding (room) temperature and the camera's indicated temperature, the aluminum emissivity may be estimated and the resulting value is $\varepsilon = 0.09 \pm 0.008$ [5].

At steady state, radiation losses (gains) from the plates are offset by convective gains (losses). If radiation is negligible, the plate temperature is equal to the average air temperature surrounding the plate (if local heat transfer coefficients about the plate are uniform). These two observations allow one to correct the measured temperature, if radiation exchange can be quantified. Radiation losses were evaluated by assuming an infinite parallel and gray plate arrangement (plate and heat exchanger surfaces) at the plate top and bottom. Then, the corrected plate temperature becomes

$$T_{\text{corrected}} = T - \sigma/(2h(2/\varepsilon - 1)) \cdot (T_t^4 + T_b^4 - 2T^4) \qquad (2)$$

where T is the measured value. The value of h (4 W m^{-2} K^{-1}) was estimated using typical mean velocities and assuming external boundary layer development over an individual plate.

All corrected temperatures are less than measured values. The corrected θ values are within 5% of the uncorrected values for plates 2–4. The corrected θ values are within 15% of the uncorrected values for plates 1 and 2 except for Case C, where the corrected values are within 25% of the uncorrected θ [5].